Impact of Quark-Gluon Plasma in Extensive Air Showers

Beatriz Artur[1,a]

[1] *Instituto Superior Técnico, Lisboa, Portugal*

Abstract. Ultra-High Energy Cosmic Rays (UHECRs) interact with the Earth's atmosphere producing *Extensive Air Showers* (EAS) at very high energies, which are not accessible at the Large Hadron Collider (LHC). The number of muons at the ground is a key observable to infer the mass composition of cosmic rays. But the data that has been collected along the years shows that the hadronic interaction models used to simulate EAS produce a muon deficit in regard to the experimental measurements. This is known as the *Muon Puzzle* and its source should be observable in high-energy collisions at the LHC. Incidentally, recent experiments with heavy-ions at the LHC have unraveled a new state of matter, called *Quark-Gluon Plasma*, which has been studied through models like the EPOS-LHC. However, this model was insufficient and so it was modified in order to phenomenologically explain the muon deficit that had been observed, originating the *EPOS-QGP*. The goal of this dissertation is to use this new model to assess if quark-gluon plasma can explain the measurements performed at the LHC and on UHECRs.

1 Theoretical Overview

The Earth is continuously bombarded by fully-ionised nuclei with relativistic kinetic energies, which are known as Cosmic Rays (CRs). The mass composition of these particles range from proton to iron, with a negligible fraction of heavier nuclei, while their energy can range from less than 1 GeV up to a few 10^{20} eV. They are labelled Ultra High-Energy (UHE) when their energy is greater than 10^{18} eV. When UHECRs reach the Earth's atmosphere and interact with air nuclei, they produce hundreds to thousands of particles, which themselves interact, triggering macroscopic cascades of secondary particles, known as Extensive Air Showers (EAS). For cosmic rays with energies greater than 10^{14} eV, their flux drops below one particle per square meter per year [1] and their extensive air showers can only be observed indirectly through ground-based experiments with huge apertures, like the Pierre Auger Observatory [2] and The Telescope Array [3]. These showers of secondary particles have two components: electromagnetic and hadronic. The electromagnetic component is mostly due to the immediate decay of neutral pions into photons ($\pi^0 \rightarrow \gamma\gamma$) and then develops independently via electron pair-production and bremsstrahlung. The hadronic core is composed by the long-lived secondary hadrons, such as baryons, charged pions and kaons. Although a small fraction of muons is produced electromagnetically by direct pair-production, 90% of the muons come from the hadronic cascade. The depth of the shower maximum (X_{max}), the number of muons at the ground (N_μ), the USP shape parameters R and L and the muon production depth maximum (X^μ_{max}) are some of the most relevant shower observables.

The Heitler-Matthews model is a simplified analytical model that approximates the air shower by a pure pion shower. This means that, after having travelled a depth corresponding to the mean interaction length λ_{int}, the initial hadron with energy E_0 produces N_π pions with energy E_0/N_π each. One-third of these particles are neutral pions, which decay immediately into photons, yielding electromagnetic subshowers, and two-thirds are charged pions $N_{\pi^\pm}$, the only ones that feed the hadronic cascade. The cascade ends when the charged particles reach a critical energy $E_{c\pi}$. Thus, X_{max} and N_μ can be written as:

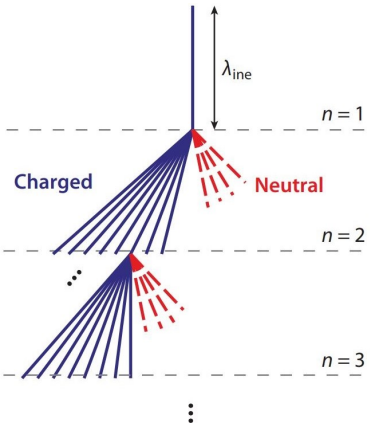

Figure 1: Simplified hadronic cascade, according to the Heitler-Mathews Model. The parameter n represents the generations and λ_{int} mean interaction length. Charged pions are represented in full lines, while neutral ones are in dashed lines. Both figures taken from [1].

$$N_\mu = A\left(\frac{E_0}{AE_{c\pi}}\right)^\beta = A^{1-\beta}\left(\frac{E_0}{E_{c\pi}}\right)^\beta, \quad (1)$$

$$X_{\max}(E_0) = \lambda_{int} + \lambda \ln\left(\frac{E_0}{AN_\pi E_c}\right), \quad (2)$$

where A is the mass of the primary, that can be though of as A independent nucleons with energy E_0/A each, and $\beta = \ln(N_{\pi^\pm})/\ln(N_\pi)$, with $N_{\pi^\pm}$ being the number of charged pions and N_π the total number of pions produced in each interaction.

Energy and composition information of the cosmic ray are derived indirectly by simulating these

[a] e-mail: beatriz.artur@tecnico.ulisboa.pt

extensive air showers and comparing the models predictions with the experimental measurements. It has been found that different models consistently predict a lower muon production. This discrepancy is known as the Muon Puzzle. To compare all the measurements from the different models, the Working group on Hadronic Interactions and Shower Physics (WHISP) introduced the abstract muon scale parameter z defined as:

$$z = \frac{\ln(N_\mu^{det}) - \ln(N_{\mu_p}^{det})}{\ln(N_{\mu_{Fe}}^{det}) - \ln(N_{\mu_p}^{det})}, \quad (3)$$

where N_μ^{det} is the muon density estimate as seen in the detector, and $N_{\mu_p}^{det}$ and $N_{\mu_{Fe}}^{det}$ are the simulated muon density estimates for proton- and iron-induced showers, accounting for detector effects, respectively [4]. Figure 2 shows the muon density measurements converted to the z-scale for the EPOS-LHC hadronic interaction model, after energy-scale cross-calibration.

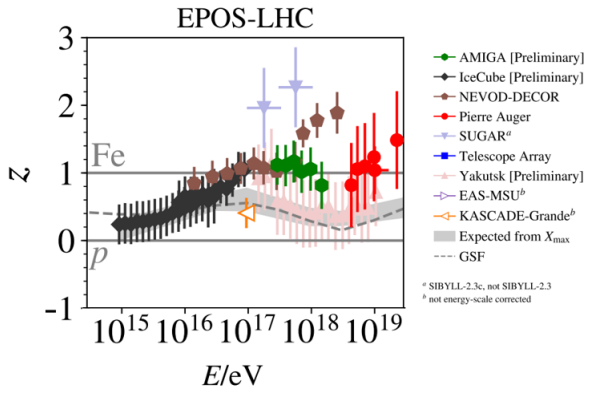

Figure 2: Muon density measurements from various experiments converted to the z scale for the EPOS-LHC hadronic interaction model, after energy-scale cross-calibration using the isotropic all-particle flux of cosmic rays as a reference. The grey band represents the expected muon-value inferred from X_{max}, while the dashed line represents the muon-value computed from the Global Spline Fit (GSF) model. Based on [4, 5].

As we can see, muon measurements seem to be consistent with simulations up to 4×10^7 GeV, which corresponds to a centre-of-mass energy of $\sqrt{s_{NN}} \approx 8$ TeV, within the reach of the Large Hadron Collider (LHC). From these energies up, there is a growing muon deficit in the simulations with a slope in z per decade in energy of 0.22, with 8σ significance. It has been proven that baryon and antibaryon production is a very efficient mechanism to affect the muon numbers in simulations without changing X_{max} [6]. In fact, a promising approach would thus be the introduction of new phenomena at high energy that could preserve the main features of the interaction while increasing the strangeness production. Such a mechanism has indeed been observed at the LHC in heavy-ion collisions - the formation of Quark Gluon Plasma.

Quark-Gluon Plasma (QGP) is a dense, energetic 'soup' made of asymptotically free quarks and gluons that manifest colour degrees of freedom on nuclear scales, but that are always very strongly coupled to each other [7, 8]. In fact, QGP exhibits a relativistic hydrodynamic fluid-like behavior with an extremely low viscosity to entropy ratio [9]. Besides being the earliest complex state of matter to form in the Universe, it can be produced in heavy-ion collisions, like the ones performed at the RHIC [10–13] and at the LHC [8, 14–17]. QGP-like phenomena appears to have been observed in various experiments spanning a wide range of densities, from dense-dense collisions (such as Pb-Pb, Au-Au and Xe-Xe) to dense-dilute (like p-Pb and He-Au) and even to dilute-dilute (namely high multiplicity pp) [8, 18]. So far, the most visible effects of a QGP presence are jet-quenching (energy loss phenomena), strangeness and baryon enhancement and anisotropic and transverse collective flow (collective elliptic flow). The visibility of these signatures is highly dependent on the centrality of the collision: the more central the collision, or, in other words, the bigger the overlap region of the two incident nuclei, the more visible are the QGP effects. Figure 3 sums up the most visible experimental signatures of QGP for each colliding system.

	Strangeness and baryon enhancement
pp	no (except high-multiplicity)
p-Pb	yes
Pb-Pb	yes
	Collectivity effects (flow)
pp	no (except high-multiplicity)
p-Pb	yes
Pb-Pb	yes
	Jet-quenching
pp	no
p-Pb	no
Pb-Pb	yes

Figure 3: Correspondence between each experimental signature of QGP and the possible colliding systems in which they have been observed, from dilute-dilute (pp) to dense-dilute (p-Pb) and dense-dense (Pb-Pb).

Note that the effect of jet-quenching in the modification of high-p_T particle production is quantified by the nuclear modification factor R_{AA}, which is given by the expression:

$$R_{AA} = \frac{dN^{AA}/dp_T}{\langle N_{coll}\rangle dN^{pp}/dp_T}, \quad (4)$$

where N^{AA} and N_{pp} are the charged-particle yields in A-A and pp collisions, respectively, and $\langle N_{coll}\rangle$ is the average number of binary nucleon-nucleon collisions. Figure 4 shows the nuclear modification factor dependence on the transverse momentum measured by the ALICE collaboration in Pb-Pb collisions at $\sqrt{s_{NN}} = 2.76$ and 5.02 TeV, for charged particles in the pseudo-rapidity region $-0.8 < \eta < 0.8$ and for the centrality class $0-5\%$. We can

see that the R_{PbPb} has a quick initial growth followed by a rapid decrease and a subsequent slow increase, always staying below unity.

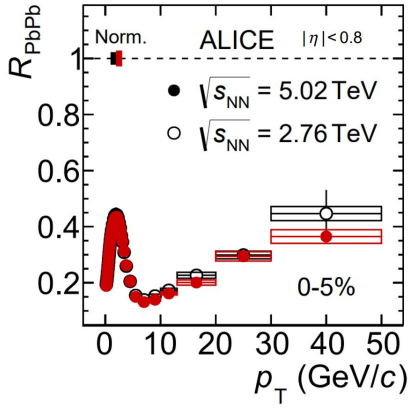

Figure 4: The nuclear modification factor dependence on the transverse momentum measured by the ALICE collaboration in Pb-Pb collisions at $\sqrt{s_{NN}}$ = 2.76 (open symbols) and 5.02 TeV (full symbols), for charged particles in the pseudo-rapidity region $-0.8 < \eta < 0.8$ and for the centrality class $0-5\%$. The boxes around unity show the normalization uncertainties. Based on [19].

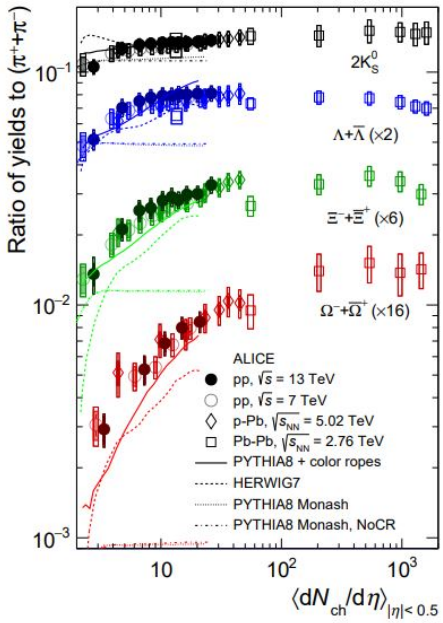

Figure 5: p_T integrated strange hadron-to-pion ratios as a function of the mean charged-particle multiplicity density measured at mid-rapidity ($|\eta| < 0.5$) for pp, p-Pb and Pb-Pb collisions. The open shaded boxes around the markers represent full systematic uncertainties (multiplicity uncorrelated). Also, different lines represent different Monte Carlo generators for pp collisions at $\sqrt{s}$ = 13 TeV. Taken from [20].

The ALICE collaboration found a universal strangeness and baryon enhancement in pp, p-Pb and Pb-Pb collisions that only depends on the multiplicity of the event at mid-rapidity, as seen in Figure 5. The source of the muon deficit should be observed in high-energy collisions at the LHC, and the most likely explanation consistent with all the available data is a small modification to the hadron production that reduces the energy fraction carried by the electromagnetic component of the shower. Such a modification would have a compounded effect on the hadronic cascade, causing large changes in the number of muons over several shower stages while leaving X_{max} and the relative muon fluctuations intact. The strangeness and baryon enhancement found by ALICE fits into the picture quite well, although its results were achieved at mid-rapidity. This means that measurements of forward hadron production at pseudo-rapidities $\eta > 2$ are needed, namely with LHCb and future data on oxygen beams at the LHC at the end of Run 3 to study p-O and O-O collisions at $\sqrt{s}$ = 10 and 7 TeV.

2 Hadron Interaction Models

Hadronic interaction models are essentially attempts to calculate hadronic multiparticle production with parameters constrained by the existing collider data and in such a consistent way that allows for a theory-guided extrapolation to ultra-high energies and to different phase-space regions than the ones explored in accelerators [1]. The leading hadronic interaction models used for air shower simulations are EPOS-LHC [21], QGSJet-II.04 [22] and SIBYLL-2.3d [23], which are all post-LHC models, but are not describing correctly all aspects of hadronic physics in air showers. In this work, we use the hadronic interaction models EPOS-LHC and EPOS-QGP along with CONEX [24, 25], which is an EAS simulation code that combines Monte Carlo simulations for the most energetic interactions with the solving of cascade equations at lower energies to simulate the longitudinal development of the shower along its axis. EPOS was the first generator to combine Parton-Based Gribov-Regge theory [26], perturbative QCD and string fragmentation with quark-gluon plasma formation to describe both small and large collision systems [27], through the use of the core-corona model [28, 29], in which an event can be divided into two parts:

- The high-multiplicity and high-energy-density core. When the string density surpasses a certain threshold, strings merge to form QGP, which then hadronizes statistically. The core dominates at mid-rapidity but also extends into the forward region, which is crucial for air shower simulations [29].
- The low-multiplicity and low-energy-density corona. If the string density stays below the threshold, the strings hadronize classically through string fragmentation, with no formation of QGP.

While QGP effects are included in EPOS-LHC, it has been shown that these appear only for very high-multiplicity events and mostly at mid-rapidity [31]. The core is produced too late compared to what is observed at the LHC and so a modified version of EPOS-LHC that

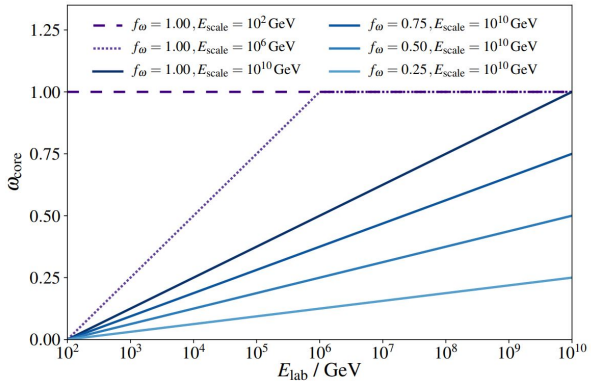

Figure 6: Energy dependence of the core weight, following equations 6 and 7, with $E_{th} = 100$ GeV and $F(E_{lab} = 0)$. E_{scale} is changed from 100 GeV to 10^6 GeV and 10^{10} GeV, and f_ω is varied by 0.25, 0.5, 0.75 and 1.0. In addition, $F(E_{lab}; E_{th}, E_{scale}) = 1$ is required for all $E_{lab} \geq E_{scale}$. Based on [30].

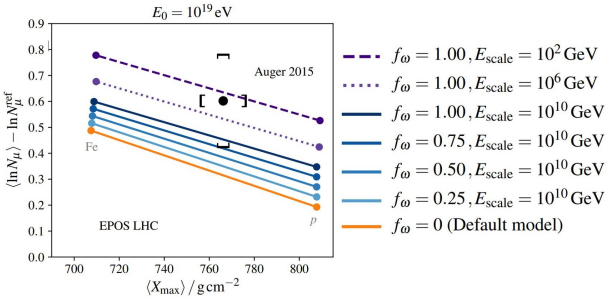

Figure 7: The average logarithm of the number of muons at the ground scaled by a reference $\ln N_\mu^{ref}$ as a function of the mean depth of the shower maximum. Different coloured lines show how the energy-dependency of the core weight explored in Figure 6 affects the relation between the two observables. Each line shows all possible values for any mass composition of 10^{19} eV cosmic rays, between pure proton (bottom right) and pure iron (top left), simulated by hadronic interaction model EPOS-LHC. Data collected by the Pierre Auger Observatory is shown in black. Based on [29].

accounts for an extended core, allowing for more visible QGP effects, was created and its called EPOS-QGP. In the phenomenological core-corona model, the particle yield N_i for particle species i is the sum of both contributions:

$$N_i = \omega_{core} N_i^{core} + (1 - \omega_{core}) N_i^{corona}, \tag{5}$$

where ω_{core} is the core weight, N_i^{core} is the particle yield if there was only core and N_i^{corona} is the particle yield if there was only corona. It is expected to increase logarithmically with energy and its energy-dependent factor is defined as:

$$F(E_{lab}; E_{th}, E_{scale}) = \frac{\log_{10}(E_{lab}/E_{th})}{\log_{10}(E_{scale}/E_{th})}, \tag{6}$$

for $E_{lab} > E_{th}$, where E_{lab} is the energy in the laboratory reference frame, E_{th} is the threshold energy above which we have core effects and E_{scale} is a reference energy scale that allows us to play with the size of the core relative to the size of the corona, marking the energy above which the core weight saturates. The energy dependence is thus modelled by:

$$\omega_{core}(E_{lab}) = f_\omega F(E_{lab}; E_{th}, E_{scale}), \tag{7}$$

where f_ω is a normalization factor that regulates the energy density of the core and its maximum weight. Relating this energy-dependence with multiplicity, in order to explain LHC data [32], ω_{core} needs to increase monotonically with the multiplicity, starting from zero for low multiplicity pp scattering, up to 0.5 or more for very high multiplicity pp and reaching unity for central heavy-ion collisions (Pb-Pb). Note that the core and corona yeilds don't depend on the multiplicity itself, but on the fraction of particles produced by the core and the corona, which leads to a smooth transition from corona yield to core yield with multiplicity. Figure 7 presents how this energy-dependence of the core weight influences the relation between two shower observables: the number of muons at the ground and the depth of the shower maximum. The EPOS-LHC predicted lines are not encompassed by the experimental data systematic uncertainty area, thus expressing the Muon Puzzle discussed in Section 1. But we can see that a higher core contribution describes the data well.

3 QGP impact in hadron interaction quantities

In order to assess the behaviour of the hadronic interaction model EPOS-QGP, we started by looking at the first interaction. Various proton- and iron-induced showers at 10^{19} eV were simulated with this model, along with proton- and iron-induced showers at the same energy using EPOS-LHC for comparison. From here onward, we denominate the proton-induced showers simulated with the hadronic interaction model EPOS-LHC as *EPOS-LHC proton*, the iron-induced showers simulated with hadronic interaction model EPOS-LHC as *EPOS-LHC iron*, and the proton-induced showers simulated with hadronic interaction model EPOS-QGP as *EPOS-QGP proton*. The number of simulated showers is 19800, 100000 and 9800, and the color code used is green (in dashed lines), magenta (in full lines) and orange (in dotted lines) for EPOS-LHC proton, EPOS-QGP proton and EPOS-LHC iron, respectively.

We looked at the multiplicity, the mean abundance of the different particle types and the x-, y- and z-momenta of the secondary particles. We concluded that almost all of the particles' momentum was along the z-direction. Moreover, EPOS-QGP produces more baryons in the first interaction than the other models, which is aligned with the baryon enhancement effect of QGP. In order to compare our findings with the existing accelerator data, especially with LHC data, we performed a Lorentz transformation to the centre-of-mass frame of the interaction, studying the z-momentum of the secondary particles, their transverse momentum and their pseudo-rapidities. We then performed cinematic cuts in the pseudo-rapidity ranges $-2 < \eta < 2$

and $-0.5 < \eta < 0.5$, where the bulk of the produced particles is concentrated. Since in this section we are mainly interested in comparing EPOS-QGP proton with EPOS-LHC proton, EPOS-LHC iron will be dropped for now. Here, we present our findings for the mean abundance of the different particle types, the transverse momentum and the nuclear modification factor, i.e. the particle yield suppression of EPOS-QGP proton with respect to EPOS-LHC proton. Figure 8 presents the mean abundance of the different types of particles produced in the first interaction, within the pseudo-rapidity cut $-2 < \eta < 2$. Both models present similar values, as seen in the ratio of their distributions in the lower plot, with neutral and charged pions being the most abundant particles. Nevertheless, EPOS-QGP proton produces more photons, neutral and charged pions, neutrons, muons, antimuons, protons and antiprotons, while EPOS-LHC proton produces more of the remaining particle types. We can thus conclude that EPOS-QGP proton produces more baryons and already about twice more muons in the first interaction than the other models, which is aligned with the baryon enhancement effect of QGP and with a possible solution to the Muon Puzzle.

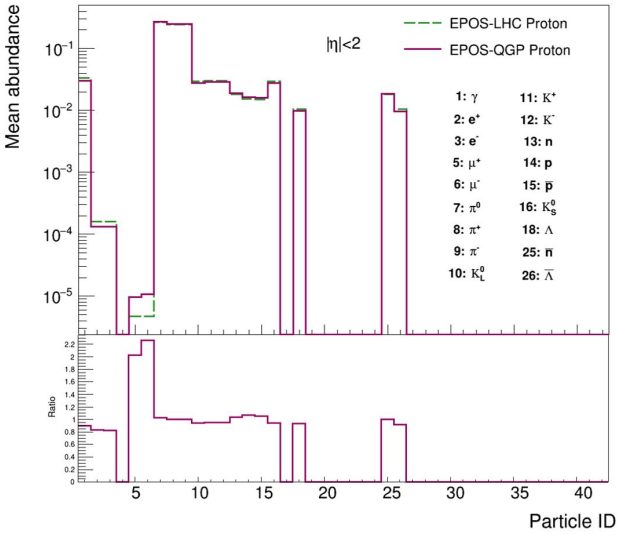

Figure 8: Mean abundance of the particles produced in the first interaction in the range $-2 < \eta < 2$, for EPOS-LHC iron (orange, dotted line), EPOS-LHC proton (green, dashed line) and EPOS-QGP proton (magenta, full line) primaries at fixed energy $\log(E/\text{eV}) = 19$. The CORSIKA numbering system is presented for an easier reading. The lower plot presents the ratio of EPOS-QGP proton distribution with respect to EPOS-LHC proton.

Figure 9 displays the distribution of the transverse momentum of the secondary particles of the first interaction in the center-of-mass frame in the mentioned kinematic cut region, normalized by the number of simulated showers. The transverse momentum is calculated through the following equation:

$$p_T = \sqrt{p_x^2 + p_y^2}. \tag{8}$$

Both models present more particles with low-p_T than with high-p_T. EPOS-QGP proton follows the distribution

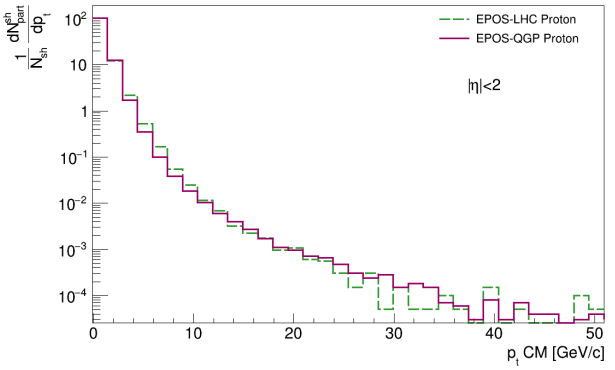

Figure 9: Distribution of the transverse momentum of the secondary particles in the center-of-mass frame and in the rapidity range $-2 < \eta < 2$, normalized by the number of simulated showers N_{sh} for EPOS-LHC proton (green, dashed line) and EPOS-QGP proton (magenta, full line) primaries at fixed energy $\log(E/\text{eV}) = 19$.

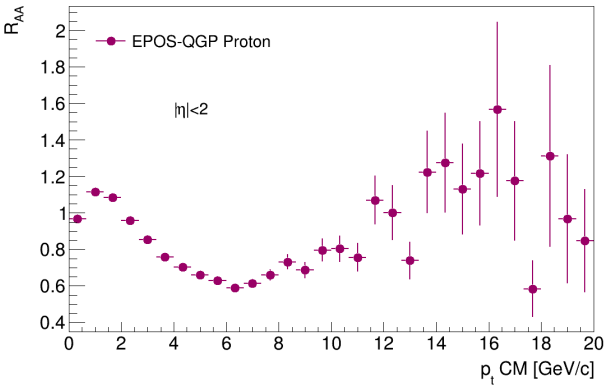

Figure 10: Nuclear modification factor dependence on the center-of-mass transverse momentum of the secondary particles, calculated for EPOS-QGP proton with respect to EPOS-LHC proton in the pseudo-rapidity region $-2 < \eta < 2$, for $\log(E/\text{eV}) = 19$ primaries.

of EPOS-LHC proton quite closely, although it produces slightly more particles with low-p_T and less particles with high-p_T than EPOS-LHC, apart from the fluctuations in the tail. This is confirmed by Figure 10, which shows the nuclear modification factor dependence on transverse momentum in the same pseudo-rapidity region. The procedure was the following: both EPOS-QGP proton and EPOS-LHC proton p_T distributions were scaled by the respective number of simulated showers and then the ratio of these quantities was performed. Compared to Figure 4, our nuclear modification factor presents the expected behaviour, with an initially growth followed by a descending curve that afterwards grows again. However, its values are different since our colliding system (p-A) is less dense and thus QGP-like effects are expected to be smaller. In fact, the low-p_T particles have an R_{AA} equal or a bit higher than 1 and the high-p_T particles have an R_{AA} smaller than one, apart from the fluctuations in the tail. We can thus conclude that EPOS-QGP proton presents more particles with a low-p_T than with a higher p_T, when compared to EPOS-

LHC proton, which is aligned with the energy loss caused by jet-quenching, associated with the presence of a QGP medium.

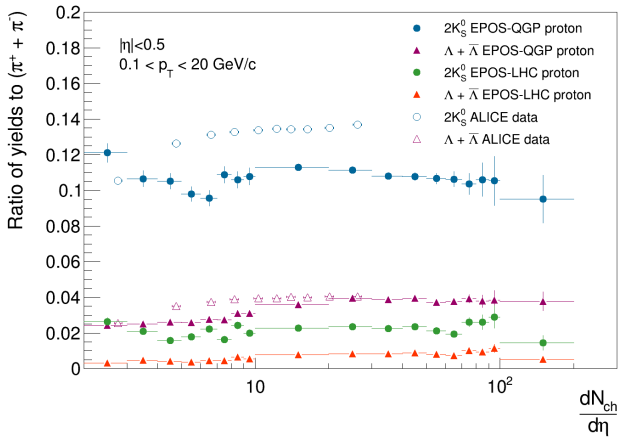

Figure 11: Strange hadron-to-pion ratios as a function of the charged-particle multiplicity density in the rapidity interval $-0.5 < \eta < 0.5$ and in the p_T interval $0.1 < p_T < 20$, for EPOS-QGP and EPOS-LHC proton primaries at fixed energy $\log(E/\text{eV}) = 19$. Data collected by the ALICE collaboration is shown in open markers [20].

Finally, to understand the strangeness production, in Figure 11 we show the ratio of strange to non-strange particles, namely $\frac{K^0_S}{\pi^\pm}$ and $\frac{\Lambda+\bar{\Lambda}}{\pi^\pm}$, as a function of the charged-particle multiplicity density in the pseudo-rapidity region $-0.5 < \eta < 0.5$ and for the p_T interval $0.1 < p_T < 20$, both for EPOS-LHC proton and for EPOS-QGP proton. These results are also compared to the ALICE findings for pp collisions at $\sqrt{s} = 13$ TeV [20], which showed an universality independent of the colliding system and of the centre-of-mass energy. The EPOS-QGP K^0_S ratio displays values compatible with the ones from the ALICE data, although the behaviour trend is not quite the same. As for the EPOS-QGP Λ+$\bar{\Lambda}$ ratios, both the values and the behavioral trend are similar to the ones from the ALICE data. In fact, both start with an increase and tend to a plateau, but EPOS-QGP exhibits a second increase along the way, reaching the same final values as the ALICE data. Curiously enough, the EPOS-LHC proton results show the exact same behavioral trend as the EPOS-QGP ones but with much lower values, not reaching the ALICE data at all. However, this discrepancy between the values reached by EPOS-LHC proton and EPOS-QGP proton shows a strangeness enhancement in the later which is compatible with the presence of a QGP medium.

4 QGP impact in air shower observables

After having evaluated the impact of EPOS-QGP on the first interaction, we studied its effects on the subsequent shower development, evaluating different shower observables, namely the depth of the shower maximum X_{max}, the number of muons at the ground N_μ and its corresponding ratio R_μ, the Universal Shower Profile (USP) shape parameters R and L and the muon production depth maximum X^μ_{max}. The same simulations mentioned in section 4 were used for the distributions of these observables and for their correlations. In addition, we also observed their energy-dependence by simulating showers in the same conditions as before, but now for the following energies: 10^{14}, 10^{15}, 10^{16}, $10^{17.5}$, 10^{18}, $10^{18.5}$, 10^{19} and $10^{19.5}$ eV for EPOS-QGP proton and EPOS-LHC proton, and $10^{17.5}$, 10^{18}, $10^{18.5}$ and 10^{19} eV for EPOS-LHC iron. Note that the study of EPOS-QGP focused only on showers with a pure proton composition for the primary, but other compositions are possible. Our findings are summarized in Figure 12, which presents the discrepancy values between EPOS-QGP proton and EPOS-LHC proton for the mean and for the fluctuations of the different shower observables, for showers with a 10^{19} eV primary.

	EPOS-QGP proton with respect to EPOS-LHC proton (E ∼ 10^{19} eV)		
	Mean	**Fluctuations**	**Comment**
X_{max}	-6.0 g cm^{-2}	+0.9 g cm^{-2}	Similar slope in the exponential tail
R	-0.004	+0.0009	-
L	+0.1 g cm^{-2}	+0.1 g cm^{-2}	-
N_μ	+13.1%	+1.3%*	Similar slope in the exponential tail
X^μ_{max}	-27.6 g cm^{-2}	0.7 g cm^{-2}	Similar slope in the exponential tail

*Relative fluctuations.

Figure 12: Systematization of the obtained results for the mean value and the fluctuations of each air shower observable, when comparing the performance of hadronic interaction models EPOS-QGP and EPOS-LHC for proton-induced showers at 10^{19} eV.

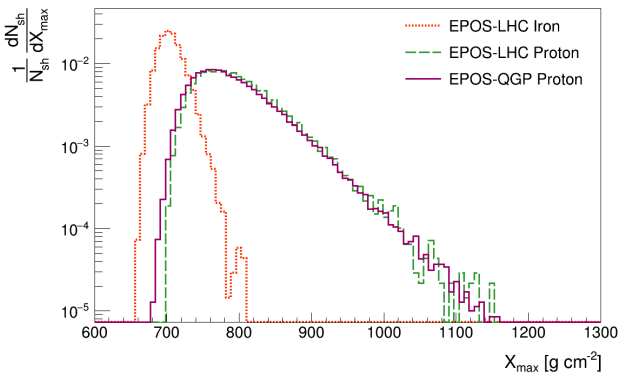

Figure 13: Distribution of the depth of the shower maximum normalized by the number of simulated showers N_{sh} for EPOS-LHC iron (orange, dotted line), EPOS-LHC proton (green, dashed line) and EPOS-QGP proton (magenta, full line) primaries at fixed energy $\log(E/\text{eV}) = 19$.

Starting with the depth of the shower maximum, Figure 13 shows its distribution and we can see that the iron-induced showers have a much narrower and lower-valued

distribution than the proton-induced ones, which complies with equation 2. In addition, EPOS-QGP proton and EPOS-LHC proton have very similar behaviours, with the former having a slightly broader X_{max} distribution by starting at lower values. This means that EPOS-QGP accounts for slightly shallower air showers than EPOS-LHC proton. The slope of the exponential tail of both models is also similar, indicating an unchanging first interaction cross-section [33, 34]. This behaviour shows how EPOS-QGP does not alter X_{max} significantly. Furthermore, Figure 14 presents the energy dependence of the average X_{max} for all the models and compares it to data collected by the Pierre Auger Observatory [35]. In all models, $\langle X_{max} \rangle$ shows a positive linear increase with the logarithm of the energy, as would be expected since X_{max} increases with the energy of the primary particle, as was seen through equation 2. This equation is also aligned with the fact that the iron-induced showers present lower average values of X_{max}. As for the proton-induced showers, EPOS-QGP and EPOS-LHC exhibit similar elongation rates but with the former presenting slightly shallower showers. Note that the data collected by the Pierre Auger Observatory is contained between the proton and iron lines.

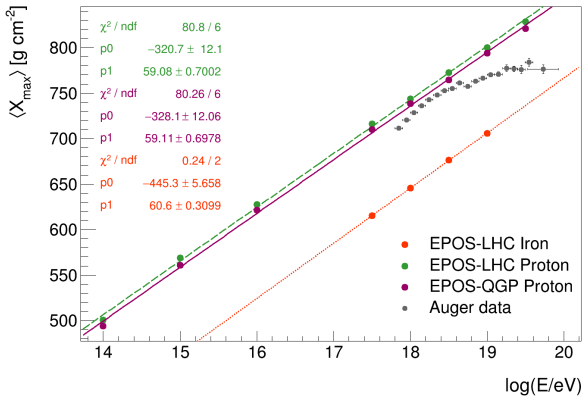

Figure 14: The average value of the depth of the shower maximum for EPOS-LHC iron (orange, dotted line), EPOS-LHC proton (green, dashed line) and EPOS-QGP proton (magenta, full line) primaries at fixed energies $\log(E/\text{eV}) = 14, 15, 16, 17.5, 18, 18.5, 19$ and 19.5. Compared with data obtained by the Pierre Auger Observatory (gray) [36]. The fits follow the line equation $\langle X_{max} \rangle = p0 + p1 \log(E/eV)$.

As for the number of muons at the ground, Figure 15 exhibits the distribution of N_μ with two fits performed for the exponential tails of EPOS-LHC proton and EPOS-QGP proton. According to equation 1, heavier primaries imply more muons at the ground, which justifies the narrower but higher-valued curve of the iron-induced showers, in comparison to EPOS-LHC proton. However, EPOS-QGP proton demonstrates a wider distribution, starting roughly in the same place as EPOS-LHC proton, growing slower, reaching a maximum a bit later and ending at higher values of N_μ. Thus, EPOS-QGP does increase the number of muons at the ground, in comparison to the other simulations. Also note that the slopes

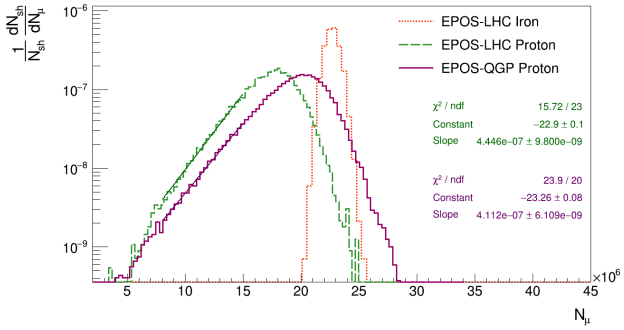

Figure 15: Distribution of the number of muons at the ground normalized by the number of simulated showers N_{sh} for EPOS-LHC iron (orange, dotted line), EPOS-LHC proton (green, dashed line) and EPOS-QGP proton (magenta, full line) primaries at fixed energy $\log(E/\text{eV}) = 19$.

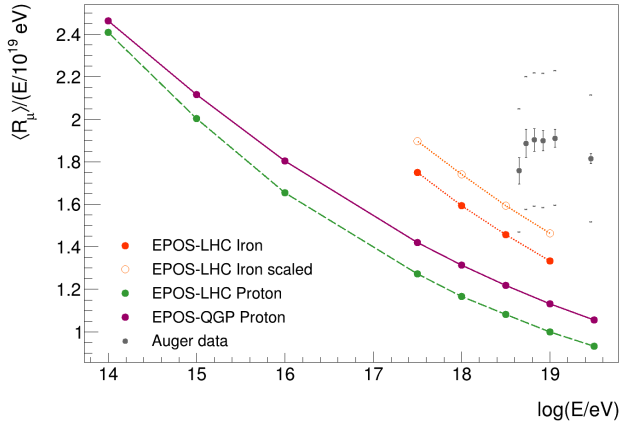

Figure 16: The mean value of the ratio $R_\mu = \frac{N_\mu}{\langle N_\mu \rangle_{p,10^{19}}}$, normalized by the energy of the shower divided by the reference energy of 10^{19} eV, in function of the shower energy for EPOS-LHC iron (orange, dotted line), EPOS-LHC proton (green, dashed line) and EPOS-QGP proton (magenta, full line) primaries at fixed energies $\log(E/\text{eV}) = 14, 15, 16, 17.5, 18, 18.5, 19$ and 19.5. A rough estimate for iron-induced showers simulated with EPOS-QGP was calculated through the difference found between EPOS-QGP proton and EPOS-LHC proton (orange, open circles). Compared with data obtained by the Pierre Auger Observatory (gray) [37].

of the exponential tail of EPOS-LHC proton and EPOS-QGP proton curves are very similar, indicating that the π^0 energy spectrum tails in the first interaction are essentially the same [38]. The Pierre Auger Collaboration [37] introduced a new parameter R_μ, given by the integrated number of muons at the ground divided by a reference related to the average number of muons in simulated proton-induced showers at 10^{19} eV. Figure 16 shows the energy dependence of the average value of R_μ, as predicted by the different models. They all show a decrease with energy, with EPOS-LHC iron exhibiting higher values of $\langle R_\mu \rangle$, as would be expected from equation 1. Comparing the proton-induced showers, EPOS-QGP exhibits higher $\langle R_\mu \rangle$ values than EPOS-LHC, which is aligned with the con-

clusion that EPOS-QGP increases the number of muons at the ground. A rough estimate was made for the results of EPOS-QGP iron-induced showers, based on the difference found between this model and EPOS-LHC proton, and one can see that this prediction overlaps the data region.

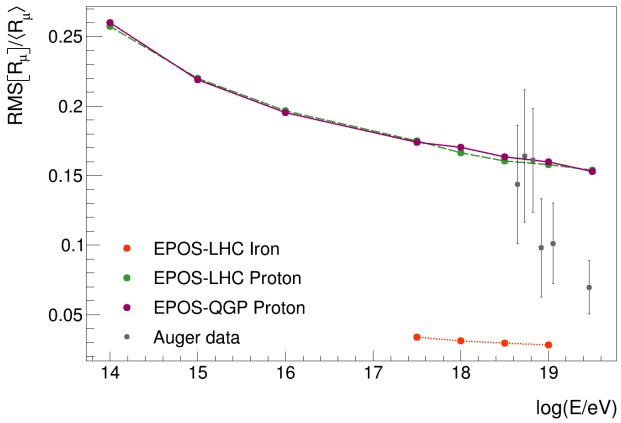

Figure 17: Relative fluctuations in the number of muons at the ground for EPOS-LHC iron (orange, dotted line), EPOS-LHC proton (green, dashed line) and EPOS-QGP proton (magenta, full line) primaries at fixed energies $\log(E/\text{eV}) = 14, 15, 16, 17.5, 18, 18.5, 19$ and 19.5. Compared with data obtained by the Pierre Auger Observatory (gray) [37].

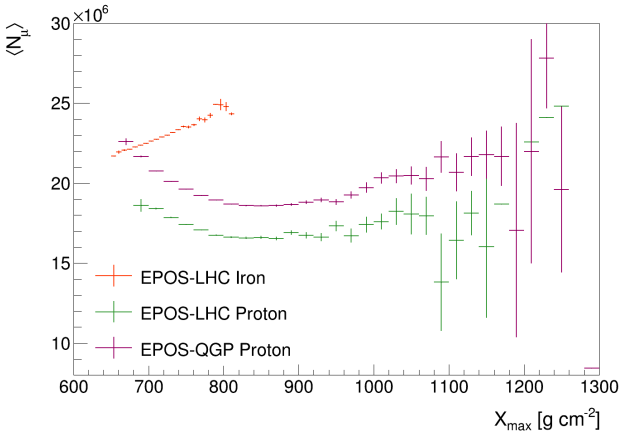

Figure 18: Mean of the number of muons at the ground for each bin of the depth of the shower maximum for EPOS-LHC iron (orange, dotted line), EPOS-LHC proton (green, dashed line) and EPOS-QGP proton (magenta, full line) primaries at fixed energy $\log(E/\text{eV}) = 19$.

The relative fluctuations in the number of muons at the ground as a function of the energy were also studied and are shown in Figure 17. EPOS-QGP does not seem to alter these fluctuations in comparison to EPOS-LHC proton, which is a condition to solve the Muon Puzzle, as discussed in section 1. EPOS-LHC iron presents much lower values, in comparison to the proton-induced showers, and the data collected by the Pierre Auger Observatory is contained between all the models lines. Figure 18 depicts the average number of muons in function of X_{max}. Heavier primaries indicate smaller X_{max} but higher N_μ, which is what we observe for EPOS-LHC iron. EPOS-QGP proton exhibits the same trend as EPOS-LHC proton. It spans the same values of X_{max}, except that it also encompasses slightly lower values, but presents higher values of N_μ. This is in line with the muon increase of EPOS-QGP that has already been observed in Figures 15 and 16.

The distributions of the USP shape parameters R and L are presented in Figures 19 and 20, respectively. R has a narrower but higher-valued distribution for iron-induced showers. EPOS-LHC and EPOS-QGP behave very similarly for proton-induced showers, with the EPOS-QGP curve starting above the EPOS-LHC one, but inverting this tendency after the peak. However, EPOS-QGP does not seem to alter R significantly. As for L, its distribution peaks roughly at the same value for all models, with iron-induced showers having a slightly narrower but lower-valued distribution, while proton-induced showers have a wider distribution, reaching higher values of L. Once again, EPOS-QGP does not seem to alter the L values significantly, with its curve basically overlapping the EPOS-LHC proton one.

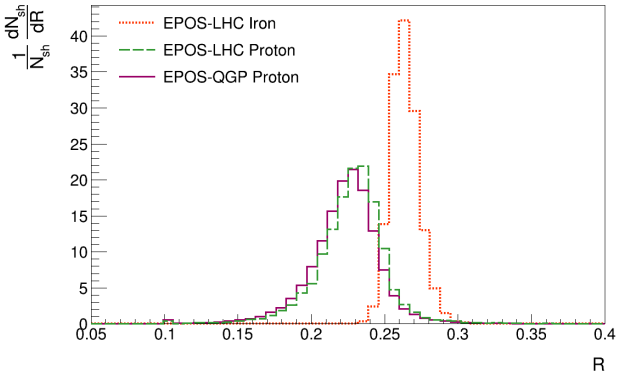

Figure 19: Distribution of the shape parameter R normalized by the number of simulated showers N_{sh} for EPOS-LHC iron (orange, dotted line), EPOS-LHC proton (green, dashed line) and EPOS-QGP proton (magenta, full line) primaries at fixed energy $\log(E/\text{eV}) = 19$.

The distribution of the muon production depth maximum is presented in Figure 21. The iron-induced showers show a narrower and lower-valued distribution, compared to the proton-induced ones, much like what was observed in the distribution of X_{max} (see Figure 13). Comparing EPOS-QGP proton with EPOS-LHC proton, they present similarly wide distributions, with the EPOS-QGP curve starting earlier and above the EPOS-LHC one, a trend that generally inverts after the peak, which is reached before for EPOS-QGP. The slope of the exponential tail of both models is also similar, indicating that the first interaction cross-section doesn't change from one model to the other [33, 34]. Thus, we can conclude that EPOS-QGP increases the number of muons at the ground and makes the muon production depth maximum happen sooner in the shower development.

Finally, we also simulated an observable that hasn't been published yet, but that might be in the future: the dif-

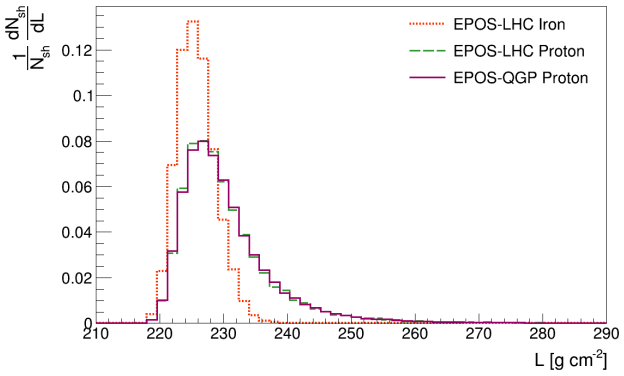

Figure 20: Distribution of the shape parameter L normalized by the number of simulated showers N_{sh} for EPOS-LHC iron (orange, dotted line), EPOS-LHC proton (green, dashed line) and EPOS-QGP proton (magenta, full line) primaries at fixed energy $\log(E/\text{eV}) = 19$.

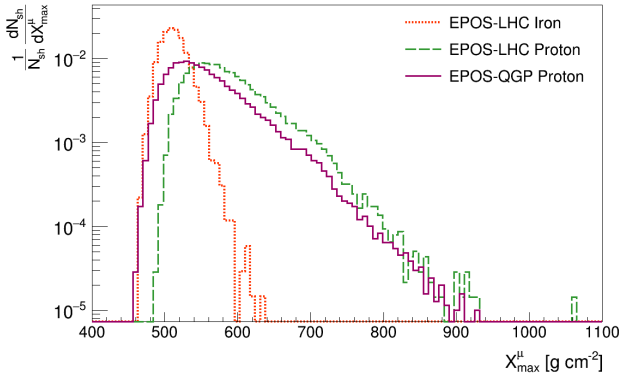

Figure 21: Distribution of the muon production depth maximum normalized by the number of simulated showers N_{sh} for EPOS-LHC iron (orange, dotted line), EPOS-LHC proton (green, dashed line) and EPOS-QGP proton (magenta, full line) primaries at fixed energy $\log(E/\text{eV}) = 19$.

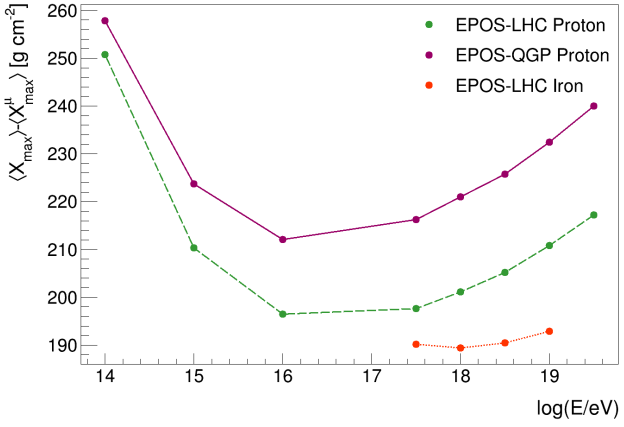

Figure 22: The difference between the mean of the muon production depth maximum and the mean of the depth of the shower maximum for EPOS-LHC iron (orange, dotted line), EPOS-LHC proton (green, dashed line) and EPOS-QGP proton (magenta, full line) primaries at fixed energies $\log(E/\text{eV}) = 14$, 15, 16, 17.5, 18, 18.5, 19 and 19.5.

ference between the mean of the muon production depth maximum and the mean of the depth of the shower maximum. The energy dependence of this observable is presented in Figure 22 for the different models. All simulations show a similar behaviour, with a decreasing trend for lower energies and an increasing trend for higher energies, always in the positive range. This means that the muon production depth is in average shallower than the depth of the shower maximum. Indeed, EPOS-LHC iron shows the lowest values of $\langle X_{max} \rangle - \langle X^{\mu}_{max} \rangle$, followed by EPOS-LHC proton and then by EPOS-QGP proton. The later seems to imitate the behaviour of EPOS-LHC proton but for higher values. Note that both X^{μ}_{max} and X_{max} depend on the depth of the first interaction X_1, hence their difference is only sensitive to the subsequent development of the shower. This means that this observable can give us information about the history of pion production.

5 Final Remarks and Conclusions

The goal of this dissertation was to assess the behaviour of hadronic interaction model EPOS-QGP, comparing it with its predecessor EPOS-LHC. In fact, EPOS-QGP was based on EPOS-LHC but was modified in a phenomenological way to show more visible QGP effects, such as baryon and strangeness enhancement. When combined with air shower simulations, like CONEX, the stronger QGP effects of EPOS-QGP should have a direct consequence: the enhancement of the number of muons produced during the shower development while maintaining the remaining shower observables intact, hence solving the infamous Muon Puzzle.

In fact, the results of the simulations performed for this work showed that EPOS-QGP is able to increase the number of muons produced during the shower development by a factor of about 13.1% with respect to EPOS-LHC proton without changing the depth of the shower maximum significantly. The remaining shower observables, such as the electromagnetic longitudinal profile, the USP shape parameters R and L and most importantly the relative fluctuations of the number of muons at the ground are also pretty much unchanged. Even the slopes of the exponential tails of the distributions of the depth of the shower maximum, of the number of muons at the ground and of the muon production depth maximum are similar to the ones exhibited by the proton-induced showers simulated with EPOS-LHC. The only significantly modified shower observable is the muon production depth maximum, which happens sooner in the shower development as a consequence of the increase in the produced number of muons.

However, is this muon enhancement related to the formation of QGP along the EAS? To answer this question, we turned to the center-of-mass frame of the interaction and confirmed a baryon and strangeness enhancement compatible with the presence of a QGP medium. We also noticed that EPOS-QGP has a tendency to produce more low-p_T particles and less high-p_T particles than EPOS-LHC, which is a signature of the jet-quenching phenomenon typical of QGP.

References

[1] R. Engel, D. Heck, T. Pierog, Annual Review of Nuclear and Particle Science **61**, 467 (2011)

[2] A. Aab et al. (Pierre Auger), Nucl. Instrum. Meth. A **798**, 172 (2015), 1502.01323

[3] T. Abu-Zayyad et al. (Telescope Array), Nucl. Instrum. Meth. A **689**, 87 (2013), 1201.4964

[4] L. Cazon (EAS-MSU, IceCube, KASCADE Grande, NEVOD-DECOR, Pierre Auger, SUGAR, Telescope Array, Yakutsk EAS Array), PoS **ICRC2019**, 214 (2020), 2001.07508

[5] H.P. Dembinski et al. (EAS-MSU, IceCube, KASCADE-Grande, NEVOD-DECOR, Pierre Auger, SUGAR, Telescope Array, Yakutsk EAS Array), EPJ Web Conf. **210**, 02004 (2019), 1902.08124

[6] T. Pierog, K. Werner, Phys. Rev. Lett. **101**, 171101 (2008), astro-ph/0611311

[7] D. LaHurd, C.E. Covault, JCAP **11**, 007 (2018), 1707.01563

[8] L. Apolinário, Y.J. Lee, M. Winn (2022), 2203.16352

[9] W. Busza, K. Rajagopal, W. van der Schee, Ann. Rev. Nucl. Part. Sci. **68**, 339 (2018), 1802.04801

[10] I. Arsene et al. (BRAHMS), Nucl. Phys. A **757**, 1 (2005), nucl-ex/0410020

[11] B.B. Back et al. (PHOBOS), Nucl. Phys. A **757**, 28 (2005), nucl-ex/0410022

[12] J. Adams et al. (STAR), Nucl. Phys. A **757**, 102 (2005), nucl-ex/0501009

[13] K. Adcox et al. (PHENIX), Nucl. Phys. A **757**, 184 (2005), nucl-ex/0410003

[14] N. Armesto, E. Scomparin, Eur. Phys. J. Plus **131**, 52 (2016), 1511.02151

[15] P. Foka, M.A. Janik, Rev. Phys. **1**, 172 (2016), 1702.07231

[16] P. Foka, M.A. Janik, Rev. Phys. **1**, 154 (2016), 1702.07233

[17] R. Bala, I. Bautista, J. Bielcikova, A. Ortiz, Int. J. Mod. Phys. E **25**, 1642006 (2016), 1605.03939

[18] (2022), 2211.04384

[19] S. Acharya et al. (ALICE), JHEP **11**, 013 (2018), 1802.09145

[20] S. Acharya et al. (ALICE), Eur. Phys. J. C **80**, 693 (2020), 2003.02394

[21] T. Pierog, I. Karpenko, J.M. Katzy, E. Yatsenko, K. Werner, Phys. Rev. C **92**, 034906 (2015), 1306.0121

[22] S. Ostapchenko, EPJ Web Conf. **52**, 02001 (2013)

[23] F. Riehn, H.P. Dembinski, R. Engel, A. Fedynitch, T.K. Gaisser, T. Stanev, PoS **ICRC2017**, 301 (2018), 1709.07227

[24] T. Bergmann, R. Engel, D. Heck, N.N. Kalmykov, S. Ostapchenko, T. Pierog, T. Thouw, K. Werner, Astropart. Phys. **26**, 420 (2007), astro-ph/0606564

[25] T. Pierog et al., Nucl. Phys. B Proc. Suppl. **151**, 159 (2006), astro-ph/0411260

[26] V.N. Gribov, Sov. Phys. JETP **26**, 414–422 (1968)

[27] J. Albrecht et al., Astrophys. Space Sci. **367**, 27 (2022), 2105.06148

[28] K. Werner, A.G. Knospe, C. Markert, B. Guiot, I. Karpenko, T. Pierog, G. Sophys, M. Stefaniak, M. Bleicher, J. Steinheimer, EPJ Web Conf. **171**, 09002 (2018), 1812.06330

[29] S. Baur, H. Dembinski, M. Perlin, T. Pierog, R. Ulrich, K. Werner (2019), 1902.09265

[30] M. Perlin, Ph.D. thesis, KIT, Karlsruhe, Karlsruher Institut für Technologie, KIT, Karlsruhe, IAP (2022)

[31] T. Pierog, S. Baur, H.P. Dembinski, R. Ulrich, K. Werner, PoS **ICRC2019**, 387 (2020)

[32] J. Adam et al. (ALICE), Nature Phys. **13**, 535 (2017), 1606.07424

[33] R. Ulrich, J. Blumer, R. Engel, F. Schussler, M. Unger, New J. Phys. **11**, 065018 (2009), 0903.0404

[34] R. Ulrich, R. Engel, S. Muller, F. Schussler, M. Unger, Nucl. Phys. B Proc. Suppl. **196**, 335 (2009), 0906.3075

[35] A. Aab et al. (Pierre Auger), Phys. Rev. D **90**, 122006 (2014), 1409.5083

[36] P. Abreu et al. (Pierre Auger), PoS **ICRC2021**, 311 (2021)

[37] A. Aab et al. (Pierre Auger), Phys. Rev. Lett. **126**, 152002 (2021), 2102.07797

[38] L. Cazon, R. Conceição, F. Riehn, Phys. Lett. B **784**, 68 (2018), 1803.05699